

Article

Preliminary Studies of Perovskite-Loaded Plastic Scintillator Prototypes for Radioactive Strontium Detection

Hara Kang ^{1,2}, Sujung Min ^{1,2}, Bumkyung Seo ², Changhyun Roh ^{2,3,*} , Sangbum Hong ^{2,*} and Jae Hak Cheong ^{1,*} 

¹ Department of Nuclear Engineering, Kyung-Hee University, Yongin-si 17104, Gyeonggi-do, Korea; mqovopm@khu.ac.kr (H.K.); sjmin@kaeri.re.kr (S.M.)

² Decommissioning Technology Research Division, Korea Atomic Energy Research Institute, Daejeon 34057, Korea; bumja@kaeri.re.kr

³ Quantum Energy Chemical Engineering, University of Science and Technology (UST), 217 Gajeong-ro, Daejeon 34113, Korea

* Correspondence: chroh@kaeri.re.kr (C.R.); sbhong@kaeri.re.kr (S.H.); jhcheong@khu.ac.kr (J.H.C.)

Abstract: Functional plastic scintillators have attracted much attention for their usefulness in on-site monitoring and detection in environments. In this study, we elucidated a highly reliable and functional plastic scintillator for detection of radioactive strontium, which means a potent perovskite-loaded polymeric scintillation material based on epoxy and 2,5-diphenyloxazole (PPO). Moreover, Monte Carlo N-Particle (MCNP) simulation was performed to optimize the thickness of a plastic scintillator for efficient strontium detection. A thickness of 2 mm was found to be the optimum thickness for strontium beta-ray detection. A newly developed plastic scintillator with 430 nm emission from perovskite loading could trigger scintillation enhancement employing potential indication of perovskite energy transfer into a photomultiplier (PMT) detector. Furthermore, the response to beta-ray emitter of ⁹⁰Sr was compared to commercial scintillator of BC-400 by exhibiting detection efficiency in the energy spectrum with a fabricated perovskite-loaded plastic scintillator. We believe that this suggested functional plastic scintillator could be employed as a radiation detector for strontium detection in a wide range of applications including decommissioning sites in nuclear facilities, nuclear security and monitoring, nonproliferation, and safeguards.

Keywords: sensor; nanomaterial; perovskite; plastic scintillator; beta-ray emitter; decommissioning; strontium detection



Citation: Kang, H.; Min, S.; Seo, B.; Roh, C.; Hong, S.; Cheong, J.H. Preliminary Studies of Perovskite-Loaded Plastic Scintillator Prototypes for Radioactive Strontium Detection. *Chemosensors* **2021**, *9*, 53. <https://doi.org/10.3390/chemosensors9030053>

Academic Editors: Yoav Broza and Norman Mark Ratcliffe

Received: 18 January 2021

Accepted: 3 March 2021

Published: 8 March 2021

Publisher's Note: MDPI stays neutral with regard to jurisdictional claims in published maps and institutional affiliations.



Copyright: © 2021 by the authors. Licensee MDPI, Basel, Switzerland. This article is an open access article distributed under the terms and conditions of the Creative Commons Attribution (CC BY) license (<https://creativecommons.org/licenses/by/4.0/>).

1. Introduction

In general, radioactive strontium as a fission product is one of the common radioisotopes found at the decommissioning sites in nuclear facilities. Additionally, ⁹⁰Sr is the most abundant radioisotope that remains in the 20–30 years later of the nuclear power plant's decommissioning sites [1]. Radiation measurements such as dosimetry and dose controls are carried out by Geiger–Muller (GM) counter, gas proportional counter, or liquid scintillation counter (LSC) by measuring the high energy beta-ray emitted by ⁹⁰Y [1–3]. Radioactive characterization for ⁹⁰Sr with decay half-life of 29 years in environments requires radiochemistry analysis and beta spectroscopy. As bremsstrahlung is generated by the interaction between the medium and the beta-ray, attentions for the human influence by the external exposure from the radioactive strontium should be paid. The chemical characteristics of the ⁹⁰Sr are similar to calcium [4], it can be accumulated in bone tissue [5], which leads to bone cancer and leukemia. Finally, ⁹⁰Y from radioactive strontium is accumulated in the pancreas, which can lead to a number of problems in the body, such as cancer [6].

Today, the scintillation detector is a popular radiation measurement method in various fields such as research and industrial areas. It has been exploited to detect the particle emitted from the nuclear fusion process of the artificial nuclear for particle and nuclear

physics research [7,8] and the cosmic-ray measurement for astrophysics [9–11]. It can also be used for environmental radiation measurement [11–16] and exploring the mineral resource [17] or explosive perception for airport security [18], medical imaging for diagnosis [19] and radiotherapy dosimetry [20], and optical devices [21–25]. Plastic scintillator has been used broadly for radiation measurement with some advantages such as short decay time, corrosion-resistance, and ease of fabrication with a large scale despite the low degree of the light yield in the decommissioning site of the nuclear facilities [26–28]. Perovskites with high atomic number (Z) have been developed to enhance high thermal and chemical stability by tuning size control and composition engineering during their manufactures [29–36], and this advantage makes perovskite available in various forms due to diameter of the particle representing unique optical and electronic characteristics by quantum effects, which makes its range of application more comprehensive [32–36]. Perovskite has broad and reabsorption-free absorption spectra that enable the selection of excitation wavelength, and a narrow (30–90 nm) and sharp emission peak can be tuned with the particle size. Especially, the lead halide perovskites have recently been developed as a new semiconductor material [37] featuring high photoluminescence quantum yield [38], and energy conversion efficiency originated from their unique characteristics [39]. These features were driven by quantum confinement effect [40] and large stokes shift [41]. Large stokes shift makes excitation and emission wavelength separated, consequently minimizing the overlap between the emission wavelengths [42–45].

In this study, we performed Monte Carlo N-Particle (MCNP) simulation to optimize the thickness of a plastic scintillator for efficient strontium detection. Additionally, the scintillation enhancement of perovskite-loaded epoxy-based nanocomposites by photoluminescence spectrum and energy spectrum was obtained from the plastic scintillator employing potential indication of perovskite energy transfer with a photomultiplier (PMT) detector by experimentally demonstrating the ability of fabricated plastic scintillator and designed device to detect and monitor radioactive strontium in environments.

2. Materials and Methods

2.1. Chemicals

All chemicals and reagents were commercial products. Epoxy (WE-300A) and hardener (WE-300B) used were purchased from Baron Tech (Kimpo, Korea). A high purity grade 2,5-Diphenyloxazole (PPO), 1,4-bis(5-phenyloxazol-2-yl) benzene (POPOP), and perovskite (CAT No. 900748) were purchased from Sigma-Aldrich (St. Louis, MO, USA).

2.2. Plastic Scintillator Fabrication

Perovskite-loaded epoxy-based plastic scintillator was fabricated through thermal polymerization method with epoxy and hardener monomer. Specifically, 10 g epoxy and 10 g hardener monomer were mixed in a bottle with PPO (0.2 wt%), POPOP (0.01 wt%), and perovskite (0.5 wt%) for characteristic evaluation and detection efficiency comparison to demonstrate the scintillation enhancement through the Förster Resonance Energy Transfer (FRET) mechanism occurring inside the scintillator. The chemical formula of perovskite used is $\text{CsPbBr}_3(\text{Cl})$ including components of PbBr_2 , CsCl , and CsBr . Table 1 shows the amounts and sorts for the fabrication of functional plastic scintillators.

Table 1. Amounts and sorts for the fabrication of functional plastic scintillators.

Plastic Scintillator	Epoxy + Hardener Monomer	PPO	POPOP	Perovskite
Epoxy/PPO/POPOP	Each 10 g	0.2 wt%	0.01 wt%	–
Epoxy/PPO/perovskite	Each 10 g	0.2 wt%	–	0.5 wt%

Perovskite-loaded epoxy-based plastic scintillator was fabricated to exhibit scintillation enhancement occurring between the plastic polymer composition. A schematic fabrication process for the functional epoxy-based plastic scintillator by loading perovskite

or POPOP is presented in Figure 1. The epoxy resin mixture was set with each of the plastic scintillator compositions, and it was thoroughly mixed by sonication for 2 h. Then, the mixture poured into the stainless planchet for bubble extraction remained in the mixture using a vacuum chamber for 2 h. The degassed mixture was then annealed at 250 °C by an electric drying oven for thermal polymerization for 3 h. Polymerization was performed when the epoxy oxirane ring (epoxy-epoxy or epoxy-hydroxyl reaction) of the epoxy monomer was opened by heat energy and finally, the monomer mixture became plastic polymer scintillators. Then, a quenching process of polymerized scintillator was done in cold water for easy de-molding from the stainless planchet.

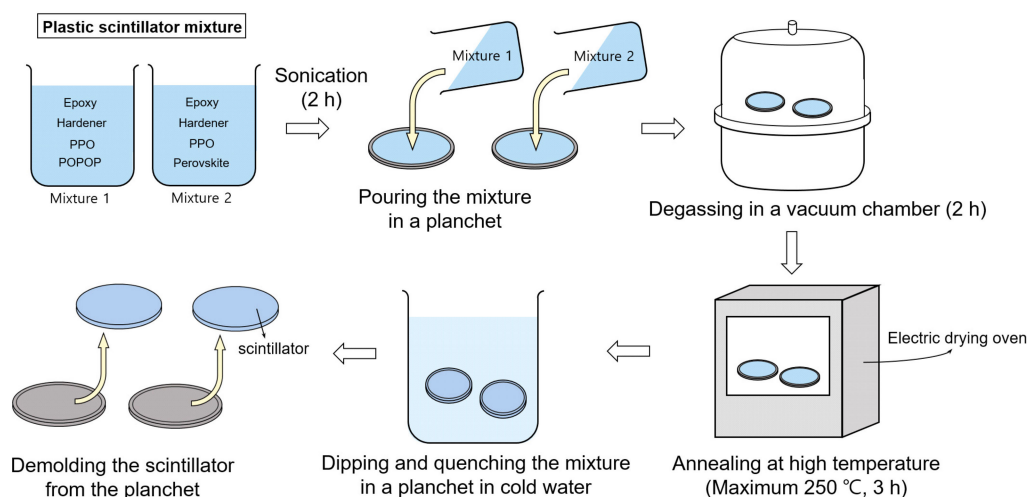


Figure 1. Schematic illustration of the fabrication process for the functional plastic scintillator. 1,4-bis(5-phenyloxazol-2-yl) benzene (POPOP) or perovskite was loaded in a mixture.

2.3. Optical and Structural Properties of the Perovskite-Loaded Epoxy-Based Scintillator

Optical and structural properties of perovskite-loaded nanocomposite polymer were analyzed; perovskite was employed to enhance the scintillation by its properties than that of the conventional wavelength shifter loaded scintillator. The scintillation mechanism from epoxy to perovskite was verified via the spectral overlap between the emission wavelength of the donor and the absorption wavelength of the acceptor. Therefore, to identify the scintillation mechanism occurring between the nanoparticles in the fabricated plastic scintillator, absorption wavelengths of the spectrums were obtained by UV-2600 (Shimadzu, Kyoto, Japan). Emission wavelengths of epoxy, PPO, POPOP, and perovskite were obtained by a spectrophoto fluorometer, Fluorolog-3 (Horiba, Kyoto, Japan). In addition, the photoluminescence intensity is compared to the POPOP or perovskite-loaded scintillator under 365 nm excitation by Fluorolog-3 (Horiba, Kyoto, Japan). The existence of the perovskite nanoparticles is identified by Transmission Electron Microscope (TEM, Tecnai G2 F30 S-TWIN, FEI Company, Hillsboro, OR, USA).

2.4. MCNP 6 Simulation for the Plastic Scintillator Thickness

For β -ray measurement, scintillator geometry optimization was deduced by the theoretical and simulation approach. The beta-ray range within the plastic scintillator can be derived by Feather's rule [46] presented as Equations (1) and (2). Equation (1) calculates the range of β -ray in the air

$$R_{max} [g/cm^2] = \begin{cases} 0.412E_{\beta}^{1.265-0.0954\ln(E_{\beta})} & 0.01 \leq E_{\beta} \leq 2.5MeV \\ 0.530E_{\beta} - 0.106 & E_{\beta} > 2.5MeV \end{cases}, \quad (1)$$

where R_{max} , E_{β} imply the maximum range of the photon in the air and energy of the beta-ray incident into the scintillator, respectively. Moreover, the beta-ray range passing through the fabricated plastic scintillator can be derived by Equation (2)

$$S = \frac{R_{max}}{\rho_{max}}, \quad (2)$$

where S , ρ_{max} imply the range of the photon passing through the scintillator medium and the density of the host matrix, respectively. Here, the density of the conventional epoxy monomer is 1.22 g/cm^2 , and 8.9 mm of the β -ray range is obtained. This value presents the maximum range of the photon passing through the medium. In addition, plastic scintillator thickness is further optimized by Monte Carlo N-Particle (MCNP) 6 computational simulation. An epoxy-based plastic scintillator, 2 mm thickness and 5 cm diameter, was simulated for geometry optimization. PMT and plastic scintillator were positioned in the fabricated optical enclosure similar to the actual experiment. Figure 2 and Figure S1 (see Supplementary Material) present the simulated experimental setup and simulation code, respectively. Experimental apparatus contained the 2-inch diameter of PMT and the planar source, scintillator, and aluminum optical enclosure. The actual component for the experiment was computationally modeled.

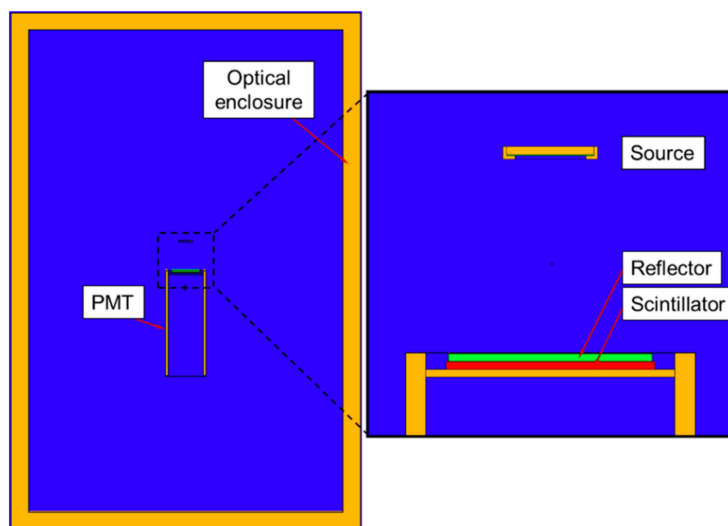
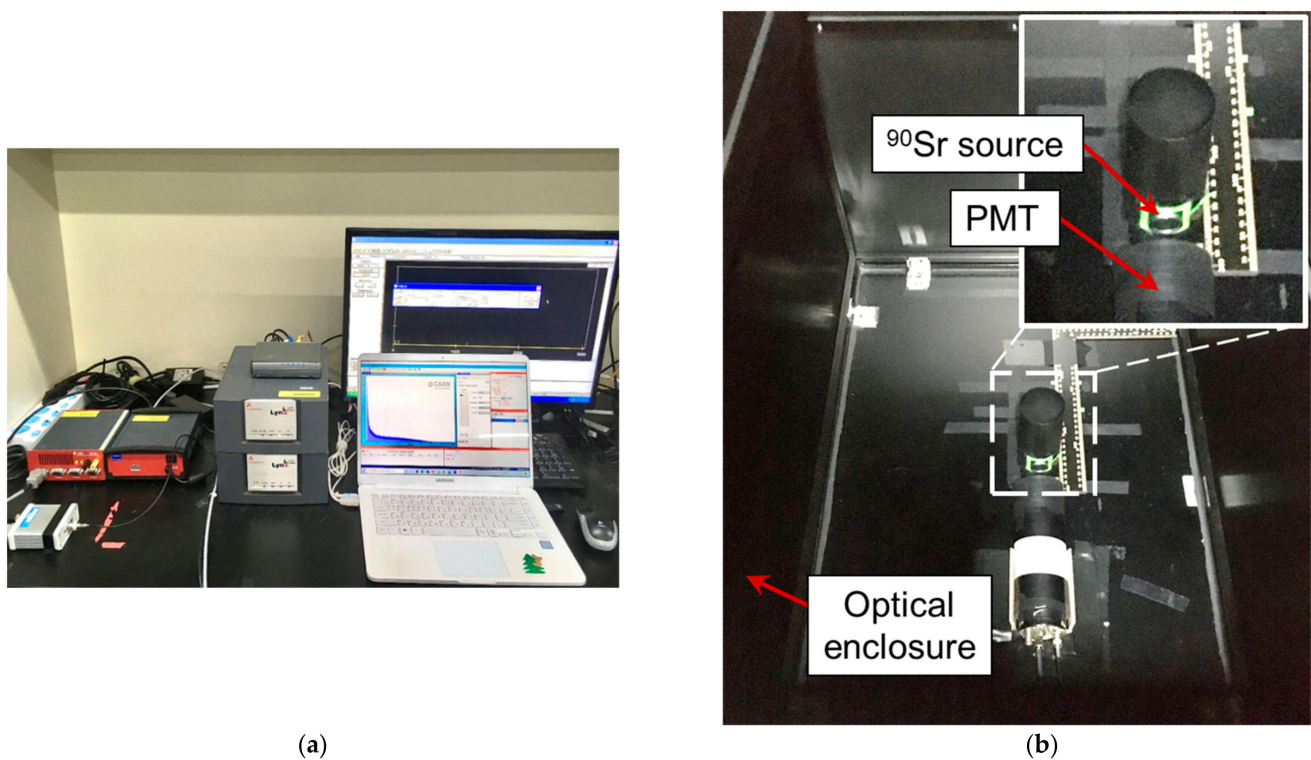


Figure 2. Monte Carlo N-Particle (MCNP) 6 simulation geometry of the experimental apparatus for β -ray measurement, which consists of a scintillator including a photomultiplier (PMT), a source and an optical enclosure.

2.5. Device Setup for Strontium Detection

For radiation measurement, a 2-inch PMT (9266B, ET enterprise, Uxbridge, England), high-voltage (Lynx, Canberra, Meriden, Australia), pre-amplifier (Amcris, Canberra), and multi-channel analyzer with an amplifier (DT5781, CAEN, Viareggio, Italy) was used (Figure 3a). The $90 \times 60 \times 45 \text{ cm}^3$ size of the aluminum optical enclosure (Atto science, Daejeon, Korea) was fabricated to minimize the interference from the light that contributes to the β -ray spectrum (Figure 3b). Additionally, the ionized β -ray measurement was carried out with a ^{90}Sr planar source as shown in Table 2.



(a)

(b)

Figure 3. Experimental apparatus set for β -ray measurement using fabricated plastic scintillators: (a) photographs of the experimental apparatus used for β -ray measurement with perovskite or POPOP-loaded scintillator based on epoxy-2,5-diphenyloxazole (PPO) and (b) the aluminum optical enclosure fabricated to reduce interference from light. The β -ray source, plastic scintillator, and PMT are equipped. Insert figure means the fabricated scintillator is attached to the PMT in the direction of a ^{90}Sr source.

Table 2. β -ray emitter exploited for radiation measurement.

Source	^{90}Sr
Activity (kBq)	18.04 Bq
β -Emax (MeV) (decay probability)	0.546/2.278

3. Results and Discussion

3.1. MCNP 6 Simulation for Scintillator Geometry Optimization

Although the range of the β -ray was obtained in the plastic medium by Feather's law, the computational simulation had been carried out for further optimization by Monte Carlo N-Particle (MCNP) 6. Figure 4 shows the result of the MCNP computational simulation calculating the β -ray range in the plastic scintillator. Moreover, 95% of energy is deposited in about 2.8 mm at ^{90}Sr source. To embrace the optimal thickness of the β -ray planar source with a different energy, 2 mm of thickness is selected.

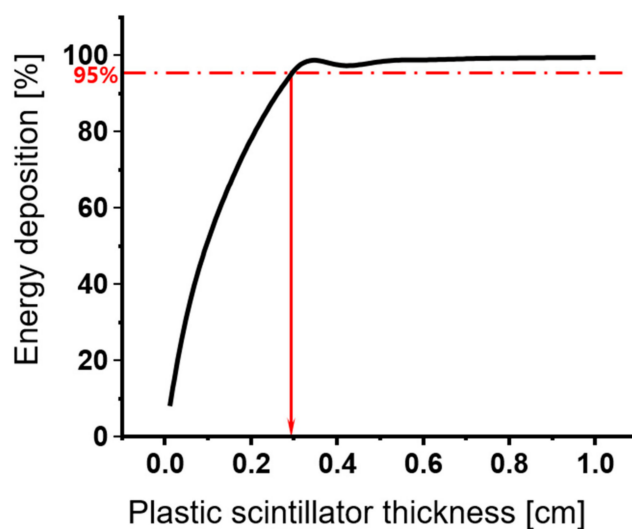


Figure 4. β -ray emitter energy deposition within the fabricated plastic scintillator simulated by MCNP 6, red-line present the 95% of energy deposition of the β -ray emitter.

3.2. Fabrication and Characterization of Epoxy-Based POPOP or Perovskite-Loaded Scintillator

Figure 5 and Figure S2 (see Supplementary Material) present the fabricated plastic scintillators. Figure 5a presents the fabricated plastic scintillator using epoxy-based scintillator including PPO and POPOP (left). Additionally, as shown in Figure 5b, the plastic scintillator on the right side consists of epoxy, PPO and perovskite. The scintillator samples with a high transparency were fabricated to a standard dimension of Φ 5 cm \times 0.2 cm as shown in Figure 5. Figure S2 shows that photoluminescence of two plastic scintillators, i.e., (a) epoxy-PPO/POPOP and (b) epoxy-PPO/perovskite, exposed by a LED Transilluminator (BLoopTM, GeneDireX, Inc., Jhunan Township, Miaoli County, Taiwan) with a maximum emission at 470 nm. As shown in Figure S2b, the epoxy-PPO/perovskite scintillator had higher photoluminescence intensity than that of other scintillator. Notably, it could be explained that the energy transfer inside the scintillator was occurred and more scintillation light was originated by the addition of the fluorescence material, PPO, and perovskite.

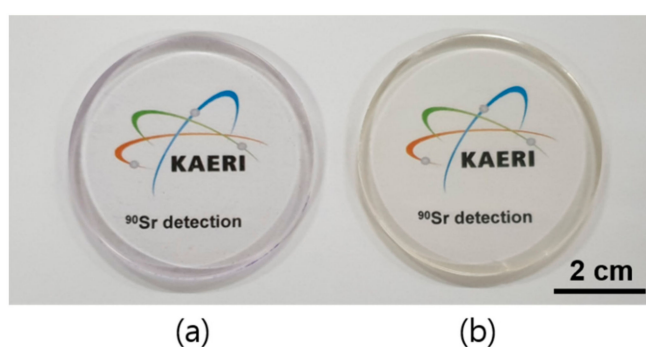


Figure 5. Fabricated plastic scintillator under light illumination: (a) epoxy matrix with PPO- and POPOP-based plastic scintillator (left) and (b) epoxy matrix with PPO and Perovskite-loaded plastic scintillator (right).

As shown in Figure 6, the absorption and photoluminescence of the fabricated scintillators were investigated. First, epoxy resin with absorption wavelength of 200–300 nm was used, as shown in Figure 6d. Second, absorbance and emission spectra of PPO and POPOP, as shown in Figure 6b,c, are similar to those reported in past literature [47]. Finally, the photoluminescence spectrum of the perovskite-loaded plastic scintillator under 374 nm excitation light is shown in Figure 6a. The peak of perovskite-loaded plastic scintillator

showed a peak approximately at 430 nm under 374 nm excitation light. Additionally, the presence of the perovskite is shown in Figure 7. The few nanometer size of the perovskite nanocrystal, which has uniform shape, are presented by TEM analysis.

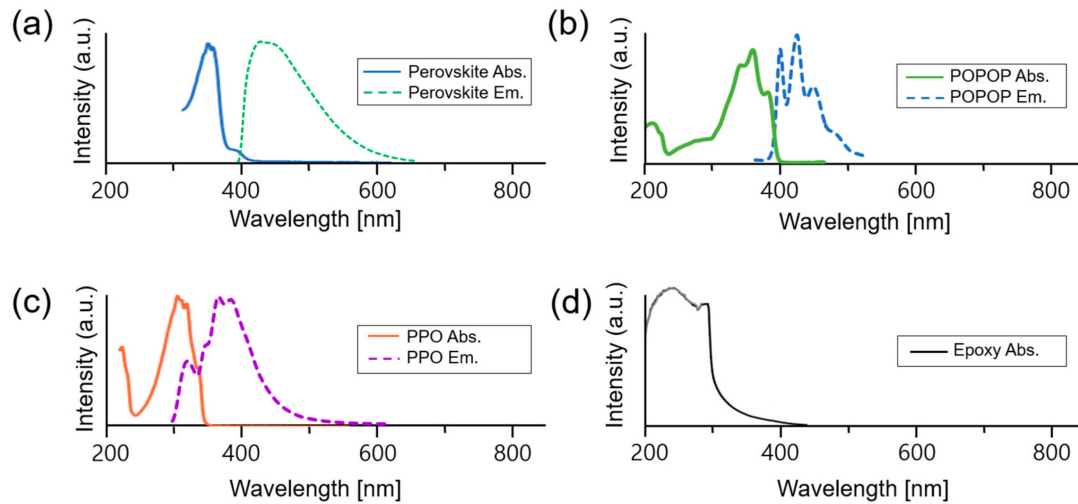


Figure 6. Absorption and emission spectra of fabricated scintillators: (a) perovskite, (b) POPOP, (c) PPO, and (d) epoxy.

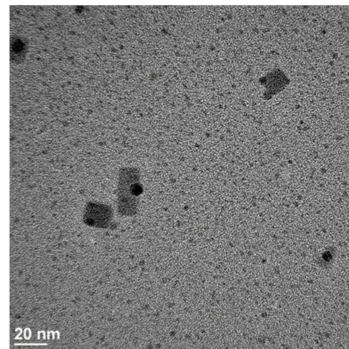


Figure 7. TEM image of the perovskite nanoparticle.

3.3. Strontium Measurement and Detection Efficiency

A total of three plastic scintillators are evaluated by radiation measurement, BC-400, epoxy-PPO/POPOP, and epoxy-PPO/perovskite. Figure 8 shows the β -ray spectrum obtained by a commercial scintillator (BC-400) and fabricated two kinds of the scintillators (epoxy-PPO/POPOP and epoxy-PPO/perovskite). Each scintillator was evaluated by radioactive strontium measurement using a ^{90}Sr β -ray planar source. The ^{90}Sr source was measured at 2 cm perpendicular to the center of the source, and a PMT detector setup with a fabricated scintillator. Each measurement is repeated three times for 30 min in real time. The dead time ranged up to 15%. BC-400, based on polyvinyl toluene, has distinct pulse-height spectrums with the epoxy-based plastic scintillator (Figure 8). This aspect comes from the polymer matrix with different densities ($\rho_{\text{PVT}} = 1.05 \text{ g/m}^3$, $\rho_{\text{Epoxy}} = 1.22 \text{ g/cm}^3$) and structural characteristics. Importantly, a slight spectrum shift and increase of the spectrum net count have been observed in epoxy-PPO/perovskite compared to epoxy-PPO/POPOP, derived from the enhancing the light yield. In the ^{90}Sr source measurement, count increment was observed in the high channel than the spectrum measured by epoxy-PPO/POPOP scintillator. This is attributed to enhanced quantum efficiency by FRET mechanism between the nanomaterials in the epoxy-PPO/perovskite plastic scintillator and reduced reabsorption rate of the emitted light due to the large Stokes shift. Possibly, the higher light intensity originated by quantum confinement effect influenced the increased

net count. The strontium spectrum for epoxy-PPO/perovskite is similar to those reported by Tam et al. based on cadmium sulfide quantum dots [48]. No extra change besides slight altitude was observed across the spectrum with low beta energy from strontium-90 decay. Moreover, the spectra collected from the scintillation counting for the different plastic scintillators are shown in Figure S3 (see Supplementary Material).

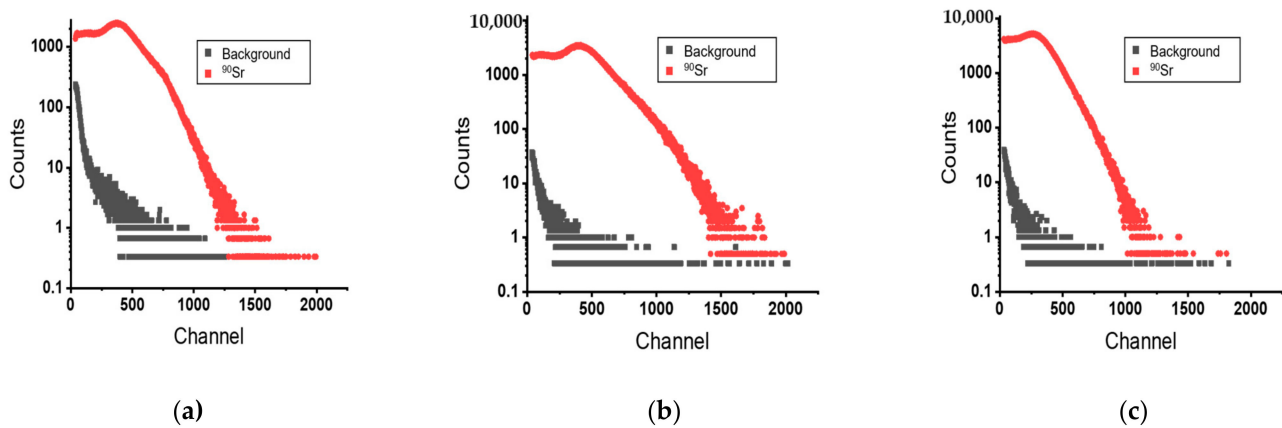


Figure 8. The spectra of three kinds of plastic scintillators obtained by a ^{90}Sr planar source for radiation measurement: (a) epoxy-PPO/POPOP, (b) epoxy-PPO/perovskite, and (c) commercial plastic scintillator (BC-400, Saint Gobain).

In addition to the individually obtained spectrum with three different kinds of plastic scintillators as shown in Figure 8, Figure 9a shows the ratio between epoxy-PPO/perovskite total counts at each channel and epoxy-PPO/POPOP total counts at each channel. Equation (3) represents the ratio of the counts for epoxy-PPO/perovskite divided by the counts for epoxy-PPO/POPOP at each channel.

$$\text{Count ratio} = \frac{\frac{\text{count of the each channel}}{\text{net count of a source}} (\text{Epoxy} - \text{PPO/perovskite})}{\frac{\text{count of the each channel}}{\text{net count of a source}} (\text{Epoxy} - \text{PPO/POPOP})}. \quad (3)$$

If the ratio has a higher value than 1, it means that the perovskite-loaded scintillator has raised the light yield in a channel than that of the POPOP-loaded one. The results have analogous deviation with the individual spectra of a count ratio profile for the measurements, as shown in Figure 9a. High energy of ^{90}Sr ($E_{\text{max}} = 2.9 \text{ MeV}$) shows increase in the count of the high channel as well as the low channel of the spectrum. This result could be attributed to the decay energies from ^{90}Sr and ^{90}Y , respectively. As the spectrum shown, the spectrum has higher counts in epoxy-PPO/perovskite scintillator than epoxy-PPO/POPOP scintillator. In detail, these results can be derived by the interaction between ionizing radiation and the perovskite-loaded plastic scintillator medium, which has a higher light yield than that of POPOP-loaded scintillator, and the event can be detected in the higher channel. Figure 9a represents mainly two peaks in the count ratio to channels from Equation (3). From two peaks of different count ratio, Figure 9b suggests different energies of the beta emitters corresponding to beta particle ^{90}Sr in lower energy and beta decay ^{90}Y in higher energy.

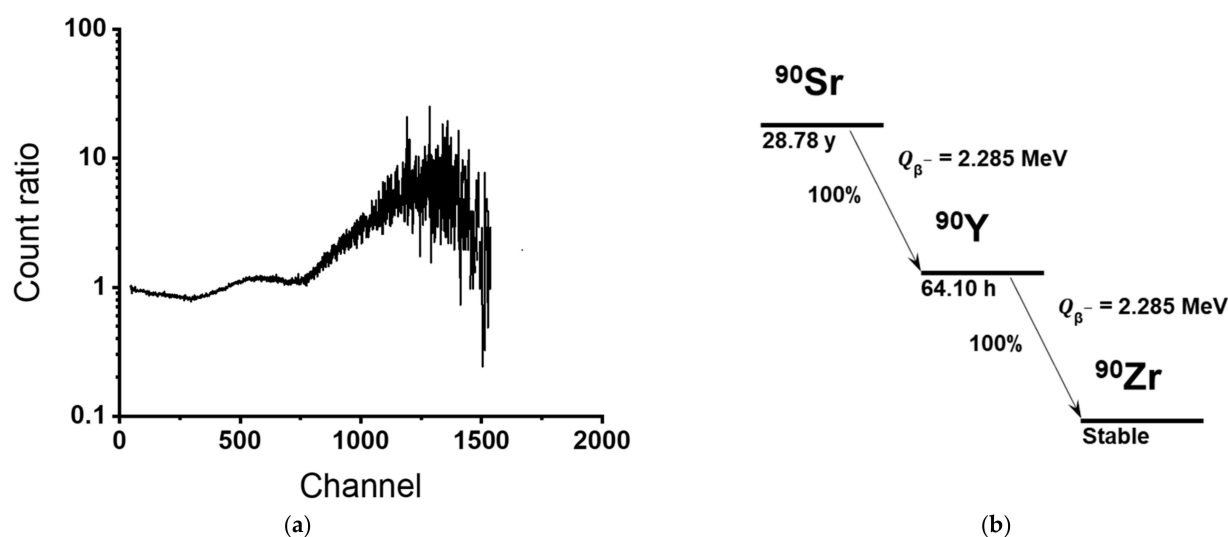


Figure 9. (a) Count ratio comparison of the ^{90}Sr planar source and (b) decay scheme for the ^{90}Sr .

Table 3 presents the compared detection efficiency of plastic scintillators. The detection efficiency of the three kinds of plastic scintillator is calculated by Equation (4).

$$\text{Detection Efficiency} = \frac{\text{net count}}{\text{radioactivity} * \text{release Probability} * \text{time}} \quad (4)$$

Detection efficiencies of the BC-400, epoxy-PPO/POPOP, and epoxy-PPO/perovskite were 20.05%, 8.58%, 17.71% for ^{90}Sr planar source, respectively. Compared to the result of the ^{90}Sr radiation measurement, relative detection efficiency of epoxy-PPO/perovskite plastic scintillator was approached to 88.3% than that of BC-400. In addition, the epoxy-PPO/perovskite plastic scintillator had more than double detection efficiency than that of the epoxy-PPO/POPOP. Moreover, standard errors obtained by the radiation measurements for pulse-height spectra are shown in Table S1 (see Supplementary Material).

Table 3. Compared detection efficiency of the plastic scintillator for β -ray emitter measurement.

source	BC-400		Epoxy-PPO/POPOP		Epoxy-PPO/Perovskite	
	Net count rate (cps)	Efficiency (%)	Net count rate (cps)	Efficiency (%)	Net count rate (cps)	Efficiency (%)
^{90}Sr	$3286 \pm 105.12\sigma$	20.05%	$1406 \pm 1.4\sigma$	8.58	$2903 \pm 49.24\sigma$	17.71

3.4. Scintillation Process and Radiation Measurement

The plastic scintillator consists of the host material as a medium and organic activator, which decide the optical properties like emission wavelength and decay time [49]. As Figure 10 presented, the general plastic scintillator consisted of three parts of the compounds. To verify the energy transfer process, the spectral overlap between the emission and absorption wavelength of each compartment consisting of the plastic scintillator was presented. Figure 6 shows absorption and emission spectrums originated by the epoxy, PPO, and perovskite. These spectrums are well engaged in meeting the condition for generating Förster resonance energy transfer. The scintillation in the two kinds of plastic scintillators, one is perovskite-loaded and the other is POPOP loaded, goes through wavelength transition sequences three times each to emit the visible photon that transfers to the PMT. The radiation from the ^{90}Sr planar source incident into the plastic scintillator initially interacts with the epoxy matrix by radiative energy transfer and is converted to the UV-photon with the wide range of the emission spectrum employing epoxy resin with absorption wavelength of 200~300, representing that shifting of the π -electrons into excited

singlet states is the major excitation process. Second, the UV-photon is then absorbed by the PPO molecules, which transfers to the POPOP or perovskite nanoparticles shortly with the emission wavelength from 350 to 400 nm. In the perovskite-loaded plastic scintillator, emission of the PPO transfer to the perovskite has a consecutive absorption spectrum (330~400 nm). Finally, the visible photons with the narrow wavelength of emission spectra (430~450 nm) are emitted. The photons emitted from the PPO are transferred to the POPOP with the other plastic scintillator, emitting the visible photons with the wavelength of 400~440 nm. It should be noted that the overlapped wavelengths between the absorption and emission spectrum of the perovskite are minuscule, while other molecules such as PPO and POPOP have the unneglectable overlap region. Among various polymer-based materials, epoxy resin has been widely used due to its transparency, high viscosity, long-term stability, and chemical resistance [47]. The low shrinkage rate and thermosetting resin property make epoxy easy to fabricate to a desirable size. As the mean free path of the converted photon from the host material is too short of matching the photodetector and fluorescence efficiency is poor, one or more scintillation additives are added. Various kinds of a compound such as *p*-terphenyl, 2,5-Diphenyloxazole (PPO), and 2,5-diphenyl-1,3,4-oxadiazole (PPD) are served as primary fluorescent compound. The plastic scintillator fabricated in this study consists of an epoxy monomer as a matrix, 2,5-Diphenyloxazole (PPO) as the first fluorescent compound, and perovskite for wavelength shifter. Here, the energy triggered beta-ray emitter of ^{90}Sr is transferred from the excited state of the epoxy to PPO through the FRET mechanism exhibiting a dipole-dipole interaction in which a non-radiative energy transfer occurs between the first excited π -singlet state of the epoxy and PPO. In addition, the primary fluorescent compound like PPO or PPD transfers its excitation energy to the secondary fluorescent compound through the emission and reabsorption of a photon. Usually, POPOP or 1-phenyl-3-mesityl-2-pyrazoline (PMP) is used as a secondary fluorescent compound [47,50]. When the external energy is absorbed in the scintillator, the energy is converted to the visible photon and collected by a photomultiplier tube. The visible photon is converted to the electrons via the photoelectron effect by hitting the cathode, and then the electrons cascaded by passing through dynodes of the PMT to display signal data like spectrum. Recently, organic-inorganic hybrid perovskites and quantum dots have emerged as a radiation measurement where functional plastic scintillator can be applied for efficient radiation detection in the form of scintillators. Kawano group evaluated scintillation properties and photoluminescence of $(\text{C}_6\text{H}_5\text{C}_2\text{H}_4\text{NH}_3)_2\text{PbBr}_4$ -layered perovskite nanocrystal in nanoporous glasses [51]. Interestingly, Yu group elucidated a type of beta-ray scintillator based on manganese-doped 2-dimensional halide perovskites and evaluated an accumulated radiation dose due to dose rate to extend beta-ray detection technology for nuclear radiation monitoring [52]. In addition, Gandini group showed poly(methyl methacrylate) PMMA-supported plastic scintillator embedding CsPbBr_3 perovskite as a high-Z sensitizer for a large Stokes shift between its absorption and emission spectra and fast emission lifetime [53]. However, their groups did not show radiation measurement like strontium detection. Importantly, a type of plastic scintillator based on perovskite is demonstrated, and radiation measurement of radioactive strontium using designed scintillators is discussed in this study by experimentally demonstrating the ability of fabricated plastic scintillator and designed device to detect and monitor radioactive strontium in environments. Importantly, more studies are needed to understand the limitations along with unclear FRET mechanism behind perovskite-loaded plastic scintillator for unique energy transfer across the components between PPO and perovskite as well as dose response works for practical applications with detector materials.

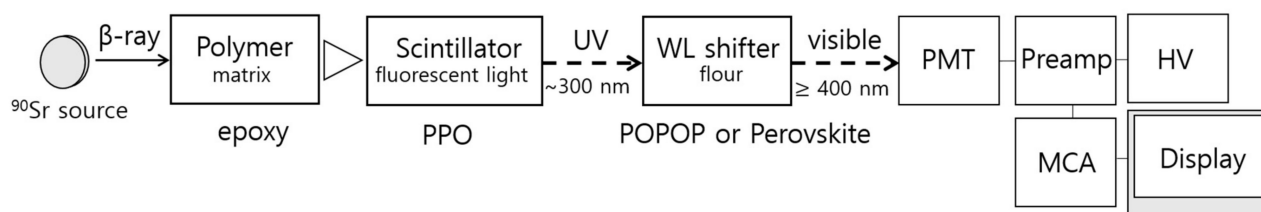


Figure 10. A simple flowchart for plastic scintillator composition, scintillation process, and radiation measurement unit with radiological processes involved for radioactive strontium beta-ray detection.

4. Conclusions

Generally, plastic scintillator materials have been employed as radiation detectors in many areas including nuclear security, nonproliferation, safeguards, and basic science and technology. In the decommissioning site, residual contamination and radioactive wastes exist, characterization is vital for managing and identifying the radiological information at the decommissioning of the nuclear facility. β -ray emitters such as ^{90}Sr is analyzed by the Geiger–Muller (GM) counter, gas proportional counter, or liquid scintillation counter (LSC). GM counter or gas proportional counter cannot detect the radioisotopes but only count the gross beta, it cannot be used for the detection. LSC has a high light output, but it is a time-consuming method from sampling to analysis. In addition, radiological contamination cannot be detected at an early stage. To compensate for these demerits of the analysis method above, a plastic scintillator with improved detection efficiency was fabricated. The perovskite-loaded nanocomposite was employed to generate Förster Resonance Energy Transfer (FRET) mechanism between the nanoparticles synthesizing the plastic scintillator. Non-radiative energy transfers from the polymer to the nanomaterial attribute to the increase of the quantum efficiency, resulting in the detection efficiency improved plastic detector. In this study, scintillation processes are taken apart with three routes. The first route goes from the epoxy matrix to wavelength shifter, perovskite. β -ray deposits its radiation energy to the matrix and generates exciton by transfer of radiative energy. They are then transported to the perovskite, where this exciton can cascade by the optical characteristics of the perovskite via non-radiative energy transfer. Otherwise, radiation energy can be directly deposited into the perovskite or the first solute material and emit the visible photon with each of their emission wavelengths. High fluorescence intensity of the epoxy-PPO/perovskite is observed, including POPOP, the conventional organic dye as a wavelength shifter, loaded scintillator inlaid eye. Furthermore, radiation measurement using radioactive strontium beta-ray source is conducted inside the fabricated aluminum optical enclosure to minimize the interference of the light. The thickness of the plastic scintillator is optimized by Feather's law and MCNP 6 simulation. The actual experimental set-up is computationally simulated as it is. Finally, plastic scintillators with 5 cm of diameter and 2 mm of thickness are fabricated for the experiment. The detection efficiency of the system with fabricated scintillator was demonstrated by representing radiation spectrum. Epoxy-PPO/perovskite had more than double the performance of the detection efficiency than that of the epoxy-PPO/POPOP, where the FRET mechanism and the upgraded quantum efficiency and light yield of the perovskite-loaded plastic scintillator are proved. The commercial plastic scintillator BC-400 is also used to compare with the fabricated scintillators. Detection efficiency of the epoxy-PPO/perovskite was reached up to 88.3% of BC-400.

In this study, we showed that perovskite nanomaterials are particularly useful because of their ability to detect beta-rays, strontium-90. Here, the beta particle type dependence results from energy transfer mechanisms that lead to or inhibit light emission, many of which are fully understood. An improved understanding of these physical mechanisms could pave the way for improving detection technology or inform the development of new materials with superior properties.

Supplementary Materials: The following are available online at <https://www.mdpi.com/2227-9040/9/3/53/s1>, Figure S1: MCNP 6 simulation code for geometry optimization of the fabricated plastic scintillator. Figure S2: Photoluminescence of two plastic scintillators exposed by a LED Transilluminator (BLoOK™, GeneDireX, Inc., Jhunan Township, Miaoli County, Taiwan) with a maximum emission at 470 nm. (a) Epoxy-PPO/POPOP and (b) Epoxy-PPO/perovskite. Figure S3. Compared radioactive strontium β -ray measurement spectrum using different plastic scintillators: (a) Epoxy-PPO/POPOP versus Epoxy-PPO/Perovskite and (b) BC-400 versus Epoxy-PPO/Perovskite. Table S1. Standard error obtained by the radiation measurement for pulse-height spectra. The measurements were repeated three times for scintillators.

Author Contributions: Conceptualization and original draft preparation: H.K., S.M., and B.S.; supervision and editing C.R., S.H., and J.H.C. All authors have read and agreed to the published version of the manuscript.

Funding: This research received no external funding.

Institutional Review Board Statement: Not applicable.

Informed Consent Statement: Not applicable.

Data Availability Statement: Data available on request from the authors.

Acknowledgments: This work was supported by a grant from the National Research Foundation of Korea (NRF), funded by the Korean government, Ministry of Science ICT (No. 2017M2A8A5015143).

Conflicts of Interest: The authors declare no conflict of interest.

References

1. Dlouhy, Z.; Crégut, A.; Genova, M.; Cross, M.T.; Reisenweaver, D.W.; Laraia, M.; Cross, M.T.; Sivintsev, Y.; Smith, R.I. *Radio-logical Characterization of Shut Down Nuclear Reactors for Decommissioning Purposes*; Technical Reports Series No. 389; IAEA: Vienna, Austria, 1998.
2. Friedli, C.; Geering, J.J.; Lerch, P. Some aspects of the behaviour of ^{90}Sr in the environment. *Radiochim. Acta* **1991**, *52–53*, 237–240. [[CrossRef](#)]
3. Putra, D.I.P.; Prihatiningsih, W.R.; Makmur, M.; Yahya, M.N.; Priasetyono, Y.; Suseno, H. A review on determination of ^{90}Sr from alkaline waters using precipitation of $\text{Ca}(\text{OH})_2$ and $\text{Ba}(\text{Ra})\text{SO}_4$. *IOP Conf. Ser. Earth Environ. Sci.* **2020**, *584*. [[CrossRef](#)]
4. Saniewski, M.; Zalewska, T. ^{90}Sr in *Zostera marina* from the Gulf of Gdańsk (southern Baltic Sea). *Oceanol. Hydrobiol. Stud.* **2017**, *46*, 24–29. [[CrossRef](#)]
5. Yoon, S.K.; Seo, H.; Lee, C.; Ahn, S.K.; Kim, H.D. *A State of the Art on Technology of Fast Neutron Measurement Based on Organic Scintillators*; Korea Atomic Energy Research Institute: DaeJeon, Korea, 2018.
6. Ferreira, C.A.; Ehlerding, E.B.; Rosenkrans, Z.T.; Jiang, D.; Sun, T.; Aluicio-Sarduy, E.; Engle, J.W.; Ni, D.; Cai, W. $^{86/90}\text{Y}$ -labeled monoclonal antibody targeting tissue factor for pancreatic cancer theranostics. *Mol. Pharm.* **2020**, *17*, 1697–1705. [[CrossRef](#)] [[PubMed](#)]
7. Naranjo, B.; Gimzewski, J.K.; Putterman, S.J. Observation of nuclear fusion driven by a pyroelectric crystal. *Nat. Cell Biol.* **2005**, *434*, 1115–1117. [[CrossRef](#)]
8. Arikawa, Y.; Yamanoi, K.; Nakazato, T.; Estacio, E.S.; Shimizu, T.; Sarukura, N.; Nakai, M.; Norimatsu, T.; Azechi, H.; Murata, T.; et al. Pr^{3+} -doped fluoro-oxide lithium glass as scintillator for nuclear fusion diagnostics. *Rev. Sci. Instrum.* **2009**, *80*, 113504. [[CrossRef](#)]
9. Del Sordo, S.; Abbene, L.; Caroli, E.; Mancini, A.M.; Zappettini, A.; Ubertini, P. Progress in the development of CdTe and CdZnTe semiconductor radiation detectors for astrophysical and medical applications. *Sensors* **2009**, *9*, 3491–3526. [[CrossRef](#)] [[PubMed](#)]
10. Osborn, J.; Fohring, D.; Dhillon, V.S.; Wilson, R.W. Atmospheric scintillation in astronomical photometry. *Mon. Not. R. Astron. Soc.* **2015**, *452*, 1707–1716. [[CrossRef](#)]
11. Undagoitia, T.M.; Von Feilitzsch, F.; Göger-Neff, M.; Hochmuth, K.; Oberauer, L.; Potzel, W.; Wurm, M. Low energy neutrino astronomy with the large liquid scintillation detector LENA. *Prog. Part. Nucl. Phys.* **2006**, *57*, 283–289. [[CrossRef](#)]
12. Milbrath, B.; Peurrung, A.; Bliss, M.; Weber, W. Radiation detector materials: An overview. *J. Mater. Res.* **2008**, *23*, 2561–2581. [[CrossRef](#)]
13. Hajagos, T.J.; Liu, C.; Cherepy, N.J.; Pei, Q. High-Z sensitized plastic scintillators: A review. *Adv. Mater.* **2018**, *30*, e1706956. [[CrossRef](#)]
14. McKigney, E.A.; Del Sesto, R.E.; Jacobsohn, L.G.; Santi, P.A.; Muenchausen, R.E.; Ott, K.C.; McCleskey, T.M.; Bennett, B.L.; Smith, J.F.; Cooke, D.W. Nanocomposite scintillators for radiation detection and nuclear spectroscopy. *Nucl. Instrum. Methods Phys. Res. Sect. A Accel. Spectrom. Detect. Assoc. Equip.* **2007**, *579*, 15–18. [[CrossRef](#)]
15. L'Annunziata, M.F. *Radioactivity*, 1st ed.; Elsevier Science: Amsterdam, The Netherlands, 2016; pp. 167–201.
16. Cerrito, L. *Radiation and Detectors*; Springer: Berlin, Germany, 2017. [[CrossRef](#)]

17. Lowdon, M.; Martin, P.G.; Hubbard, M.; Taggart, M.; Connor, D.T.; Verbelen, Y.; Sellin, P.; Scott, T.B. Evaluation of Scintillator Detection Materials for Application within Airborne Environmental Radiation Monitoring. *Sensors* **2019**, *19*, 3828. [[CrossRef](#)]
18. Miller, T.G.; Makky, W.H. Application of fast neutron spectroscopy/radiography to airport security. *Soc. Opt. Photon.* **1993**, 184–196. [[CrossRef](#)]
19. Kang, Z.; Zhang, Y.; Menkara, H.; Wagner, B.K.; Summers, C.J.; Lawrence, W.; Nagarkar, V. CdTe quantum dots and polymer nanocomposites for x-ray scintillation and imaging. *Appl. Phys. Lett.* **2011**, *98*, 181914. [[CrossRef](#)] [[PubMed](#)]
20. Buranurak, S.; Andersen, C.E. Fiber optically coupled radioluminescence detectors: A short review of key strengths and weaknesses of BCF-60 and Al₂O₃:C scintillating-material based systems in radiotherapy dosimetry applications. *J. Phys. Conf. Ser.* **2017**, *860*, 12028. [[CrossRef](#)]
21. Chen, Q.; Wu, J.; Ou, X.; Huang, B.; Almutlaq, J.; Zhumekenov, A.A.; Guan, X.; Han, S.; Liang, L.; Yi, Z.; et al. All-inorganic perovskite nanocrystal scintillators. *Nat. Cell Biol.* **2018**, *561*, 88–93. [[CrossRef](#)]
22. Yin, W.-J.; Yang, J.-H.; Kang, J.; Yan, Y.; Wei, S.-H. Halide perovskite materials for solar cells: A theoretical review. *J. Mater. Chem. A* **2014**, *3*, 8926–8942. [[CrossRef](#)]
23. Shang, Y.; Ning, Z. Colloidal quantum-dots surface and device structure engineering for high-performance light-emitting diodes. *Natl. Sci. Rev.* **2017**, *4*, 170–183. [[CrossRef](#)]
24. Lim, J.; Bae, W.K.; Kwak, J.; Lee, S.; Lee, C.; Char, K. Perspective on synthesis, device structures, and printing processes for quantum dot displays. *Opt. Mater. Express* **2012**, *2*, 594–628. [[CrossRef](#)]
25. Shirasaki, Y.; Supran, G.J.; Bawendi, M.G.; Bulović, V. Emergence of colloidal quantum-dot light-emitting technologies. *Nat. Photon.* **2012**, *7*, 13–23. [[CrossRef](#)]
26. Lee, U.; Choi, W.N.; Kim, M.J.; Kim, H.R. In situ beta radiation monitoring system with enhanced efficiency for water samples from decommissioned nuclear environment. *Rev. Sci. Instrum.* **2019**, *90*, 025103. [[CrossRef](#)] [[PubMed](#)]
27. Cieślak, M.; Gamage, K.; Glover, R.; Taylor, C. Pulse shape discrimination performance of a pixelated plastic scintillator (EJ-299-34) for a coded-aperture based dual particle imaging system. *J. Instrum.* **2019**, *14*, P07017. [[CrossRef](#)]
28. LaPlace, T.; Goldblum, B.; Brown, J.; Bleuel, D.; Brand, C.; Gabella, G.; Jordan, T.; Moore, C.; Munshi, N.; Sweger, Z.; et al. Low energy light yield of fast plastic scintillators. *Nucl. Instrum. Methods Phys. Res. Sect. A Accel. Spectrom. Detect. Assoc. Equip.* **2020**, *954*, 161444. [[CrossRef](#)]
29. Sutton, R.J.; Eperon, G.E.; Miranda, L.; Parrott, E.S.; Kamino, B.A.; Patel, J.B.; Hörantner, M.T.; Johnston, M.B.; Haghighirad, A.A.; Moore, D.T.; et al. Bandgap-tunable cesium lead halide perovskites with high thermal stability for efficient solar cells. *Adv. Energy Mater.* **2016**, *6*. [[CrossRef](#)]
30. Zhou, Y.; Zhao, Y. Chemical stability and instability of inorganic halide perovskites. *Energy Environ. Sci.* **2019**, *12*, 1495–1511. [[CrossRef](#)]
31. Guhrenz, C.; Benad, A.; Ziegler, C.; Haubold, D.; Gaponik, N.; Eychmüller, A. Solid-state anion exchange reactions for color tuning of CsPbX₃ perovskite nanocrystals. *Chem. Mater.* **2016**, *28*, 9033–9040. [[CrossRef](#)]
32. Jin, Y.; Sun, Y.; Wang, K.; Chen, Y.; Liang, Z.; Xu, Y.; Xiao, F. Long-term stable silver nanowire transparent composite as bottom electrode for perovskite solar cells. *Nano Res.* **2017**, *11*, 1998–2011. [[CrossRef](#)]
33. Cho, H.; Jeong, S.-H.; Park, M.-H.; Kim, Y.-H.; Wolf, C.; Lee, C.-L.; Heo, J.H.; Sadhanala, A.; Myoung, N.; Yoo, S.; et al. Overcoming the electroluminescence efficiency limitations of perovskite light-emitting diodes. *Science* **2015**, *350*, 1222–1225. [[CrossRef](#)]
34. Hoogland, S.; Sukhovatkin, V.; Howard, I.; Cauchi, S.; Levina, L.; Sargent, E.H. A solution-processed 1.53 μm quantum dot laser with temperature-invariant emission wavelength. *Opt. Express* **2006**, *14*, 3273–3281. [[CrossRef](#)]
35. Adachi, M.M.; Fan, F.; Sellan, D.P.; Hoogland, S.; Voznyy, O.; Houtepen, A.J.; Parrish, K.D.; Kanjanaboos, P.; Malen, J.A.; Sargent, E.H. Microsecond-sustained lasing from colloidal quantum dot solids. *Nat. Commun.* **2015**, *6*, 8694. [[CrossRef](#)]
36. Chen, C.W.; Wu, D.Y.; Chan, Y.C.; Lin, C.C.; Chung, P.H.; Hsiao, M.; Liu, R.S. Evaluations of the chemical stability and cy-toxicity of CuInS₂ and CuInS₂/ZnS core/shell quantum dots. *Phys. Chem.* **2015**, *119*, 2852.
37. Zhang, M.; Zheng, Z.; Fu, Q.; Chen, Z.; He, J.; Zhang, S.; Yan, L.; Hu, Y.; Luo, W. Growth and characterization of all-inorganic lead halide perovskite semiconductor CsPbBr₃ single crystals. *CrystEngComm* **2017**, *19*, 6797–6803. [[CrossRef](#)]
38. Richter, J.M.; Abdi-Jalebi, M.; Sadhanala, A.; Tabachnyk, M.; Rivett, J.P.; Pazos-Outón, L.M.; Gödel, K.C.; Price, M.B.; Deschler, F.A.; Friend, R.H. Enhancing photoluminescence yields in lead halide perovskites by photon recycling and light out-coupling. *Nat. Commun.* **2016**, *7*, 13941. [[CrossRef](#)]
39. Miao, Y.; Ke, Y.; Wang, N.; Zou, W.; Xu, M.; Cao, Y.; Sun, Y.; Yang, R.; Wang, Y.; Tong, Y.; et al. Stable and bright formamidinium-based perovskite light-emitting diodes with high energy conversion efficiency. *Nat. Commun.* **2019**, *10*, 1–7. [[CrossRef](#)] [[PubMed](#)]
40. Schmidt, L.C.; Pertegás, A.; González-Carrero, S.; Malinkiewicz, O.; Agouram, S.; Espallargas, G.M.; Bolink, H.J.; Galian, R.E.; Pérez-Prieto, J. Nontemplate synthesis of CH₃NH₃PbBr₃ perovskite nanoparticles. *J. Am. Chem. Soc.* **2014**, *136*, 850–853. [[CrossRef](#)]
41. Mary, V.C.V.; Rajeev, K.K.; Jayaraj, M.K. Stokes shift engineered, stable core-shell perovskite nanoparticle—poly(methylmethacrylate) composites with high photoluminescence quantum yield. *Opt. Mater.* **2019**, *94*, 241–248. [[CrossRef](#)]
42. Liu, J.; Xue, Y.; Wang, Z.; Xu, Z.-Q.; Zheng, C.; Weber, B.; Song, J.; Wang, Y.; Lu, Y.; Zhang, Y.; et al. Two-dimensional CH₃NH₃PbI₃ perovskite: Synthesis and optoelectronic application. *ACS Nano* **2016**, *10*, 3536–3542. [[CrossRef](#)] [[PubMed](#)]
43. Wang, H.-C.; Bao, Z.; Tsai, H.-Y.; Tang, A.-C.; Liu, R.-S. Perovskite quantum dots and their application in light-emitting diodes. *Small* **2017**, *14*. [[CrossRef](#)]

44. Alivisatos, A.P. Semiconductor clusters, nanocrystals, and quantum dots. *Science* **1996**, *271*, 933–937. [[CrossRef](#)]
45. Protesescu, L.; Yakunin, S.; Bodnarchuk, M.I.; Krieg, F.; Caputo, R.; Hendon, C.H.; Yang, R.X.; Walsh, A.; Kovalenko, M.V. Nanocrystals of cesium lead halide perovskites (CsPbX₃, X = Cl, Br, and I): Novel optoelectronic materials showing bright emission with wide color gamut. *Nano Lett.* **2015**, *15*, 3692–3696. [[CrossRef](#)] [[PubMed](#)]
46. Marshall, E.T.; Vaziri, K.; Krueger, F.P.; Cossairt, J.D. Determination of the secondary electron equilibrium using an extrapolation chamber (FNAL/C-96/318). In Proceedings of the Health Physics Society 1997 Midyear Topical Meeting, San Jose, CA, USA, 5–8 January 1997; Volume 28, p. 12.
47. Nam, J.S.; Choi, Y.S.; Hong, S.B.; Seo, B.K.; Moon, J.K.; Choi, J.W. Study on the characteristics of a scintillator for beta-ray detection using epoxy resin. *EPJ Web Conf.* **2017**, *153*, 07005. [[CrossRef](#)]
48. Tam, A.K.; Boyraz, O.; Unangst, J.; Nazareta, P.; Schreuder, M.; Nilsson, M. Quantum-dot doped polymeric scintillation material for radiation detection. *Radiat. Meas.* **2018**, *111*, 27–34. [[CrossRef](#)]
49. Kessler, M.J. *Liquid Scintillation Analysis*; PerkinElmer: Waltham, MA, USA, 2015.
50. Bowen, M.; Majewski, S.; Pettey, D.; Walker, J.; Wojcik, R.; Zorn, C. A new radiation-hard plastic scintillator. *Nucl. Instrum. Methods Phys. Res. Sec. A Accel. Spectrom. Detect. Assoc. Equip.* **1989**, *276*, 391–393. [[CrossRef](#)]
51. Kawano, N.; Shinozaki, K.; Nakauchi, D.; Kimura, H.; Yanagida, T. Scintillation properties of organic–inorganic layered perovskite nanocrystals in glass. *J. Appl. Phys.* **2020**, *127*, 213103. [[CrossRef](#)]
52. Yu, D.; Wang, P.; Cao, F.; Gu, Y.; Liu, J.; Han, Z.; Huang, B.; Zou, Y.; Xu, X.; Zeng, H. Two-dimensional halide perovskite as β -ray scintillator for nuclear radiation monitoring. *Nat. Commun.* **2020**, *11*, 1–10. [[CrossRef](#)] [[PubMed](#)]
53. Gandini, M.; Villa, I.; Beretta, M.; Gotti, C.; Imran, M.; Carulli, F.; Fantuzzi, E.; Sassi, M.; Zaffalon, M.; Brofferio, C.; et al. Efficient, fast and reabsorption-free perovskite nanocrystal-based sensitized plastic scintillators. *Nat. Nanotechnol.* **2020**, *15*, 462–468. [[CrossRef](#)] [[PubMed](#)]